Towards the Fabrication of Suspended Superconductor-Graphene-Superconductor Josephson Junctions

by

Haofei Wei

Submitted to the Department of Physics
in partial fulfillment of the requirements for the degree of

Bachelor of Science in Physics

at the

MASSACHUSETTS INSTITUTE OF TECHNOLOGY

June 2011

Author . . . . . .
Department of Physics

Certified by . . . . . .
Pablo Jarillo-Herrero
Assisstant Professor
Thesis Supervisor

Accepted by . . . . . .
Nergis Mavalvala
Senior Thesis Coordinator, Department of Physics

Towards the Fabrication of Suspended Superconductor-Graphene-Superconductor Josephson Junctions

by

Haofei Wei

Submitted to the Department of Physics
on May 6, 2011, in partial fulfillment of the
requirements for the degree of
Bachelor of Science in Physics

Abstract

Graphene, a newly discovered material, has been the subject of much experimental and theoretical study due to its unique electronic behavior. In this thesis, I present my work with graduate student Joel Wang to design and fabricate Josephson junctions on high quality graphene samples. Using niobium, with its high critical magnetic field, as the superconducting contact metal, along with high mobility suspended graphene samples, we hope to measure the behavior of graphene Josephson junctions in the quantum Hall regime. However, difficulties involved in the suspension and annealing processes of fabricating suspended graphene Josephson junctions have made it necessary for us to to develop a new fabrication process for making suspended Josephson devices. Over the course of this project, we have developed a fabrication process which uses a flip-chip bonder and graphene deposited on PMMA films to make suspended graphene samples. With these suspended flakes, we have produced niobium-graphene-niobium Josephson junctions which exhibit multiple Andreev reflection at temperatures of 4 K, and a Dirac peak near -0.4 V, all without any annealing of the graphene. We have also developed an annealing and lithography process which can clean graphene and preserve its cleaness during the rest of the fabrication process. This annealing process has yielded suspended graphene samples with mobility upwards of $200,000$ cm^2 V^{-1} s^{-1}, comparable with high mobility flakes presented in literature.

Thesis Supervisor: Pablo Jarillo-Herrero
Title: Assisstant Professor

Acknowledgments

I would first like to thank Professor Pablo Jarillo-Herrero for giving me the chance to work in his laboratory, and for helping me in both my research as well as my graduate school and fellowship application processes. I also want to thank Joel Wang, the graduate student whose project I was a member of, for making my research experience a fun and educational one. Thanks also to all the other members of the Jarillo-Herrero group for being such friendly and helpful people. I greatly enjoyed my time as a member of the group, and miss you all.

A big thank you to all of my friends who helped me get through MIT, and all of the MIT faculty members who have helped me get to where I am today.

Finally, the biggest thanks go to my parents, for, well, everything.

Contents

List of Figures

Chapter 1

Introduction

Approximately 70 years ago, prominent theoretical physicists Lev Landau and Rudolf Peierls argued that two-dimensional crystals are not thermodynamically stable structures [20] [27], a view later extended by Nathaniel Mermin [22] and supported by the fact that no two-dimensional crystals have been isolated. However, the discovery of graphene in 2003 [25] overturned years of conventional understanding and has even yielded a Nobel Prize in physics for its discoverers, Andre Geim and Konstantin Novoselov. Graphene is a flat, atomically-thin hexagonal lattice made up of carbon atoms. These layers form the building blocks of graphite, a common material made up of many layers of graphene. While graphite is not a system of great interest to physicists, graphene in contrast has a wealth of interesting physical properties. One of the most interesting properties of graphene is that charge carriers inside it behave as mass chiral relativist particles [5], making it the first low-energy model system for studying (2+1) dimensional quantum electrodynamcis. Aside from its unique electronic properties, graphene can also become superconducting through proximity to a superconductor via the Josephson effect. Thus, graphene Josephson junctions enable us to study the rare intersection of relativity and superconductivity, which yields such interesting results as specular Andreev reflection and the relativistic Josephson effect. By adding a strong magnetic field, we can put the Josephson junctions into the quantum Hall regime, where current is carried along edge modes instead of through the bulk of the graphene, an exciting regime not yet probed by experiment.

1.1 Experiment Overview

To study the superconducting properties of graphene in the quantum Hall regime, we use transport measurements to study the transport properties of Cooper pairs in quantum Hall edge states in graphene. The high mobility of suspended graphene, combined with the high critical magnetic field of our niobium leads, should enable us to observe observe quantum Hall edge states at a low enough magnetic field for the niobium leads to remain superconducting. However, graphene Josephson junctions are highly delicate, and the etching of niobium by hydrofluoric acid, the standard etchant used to create suspended graphene devices [6], means we cannot create suspended devices without destroying the contact between the metallic leads and graphene and makes the interface opaque to the tunneling of Cooper pairs. In addition, heat annealing of suspended graphene causes ripples in graphene which reduce the mobility and overall quality of graphene, and current annealing of graphene Josephson junctions also makes the graphene-metal interface opaque to Cooper pairs. All of these are obstacles which must be overcome if we wish create high quality Josephson junction devices which can measure the transport properties of Cooper pairs in graphene while in the quantum Hall regime. The purpose of this project was to develop a method to fabricate niobium-graphene-niobium Josephson junctions using suspended graphene, so we can perform the desired measurements.

1.2 Thesis Outline

In chapter one of this thesis, I will present an overview of the theory of graphene, including its crystalline and electronic structure. In chapter two, I will present the theory of graphene Josephson junctions. In chapter three, I will discuss the various fabrication techniques we developed for producing suspended graphene Josephson devices. In chapter four, I will present the measurements we used to study our Josephson juctions and the data resulting from those measurements. Finally, in chapter five, I will summarize the results of the experiment and discuss the future directions of the

experiment.

Chapter 2

Basics of Graphene Theory

2.1 Crystalline Structure

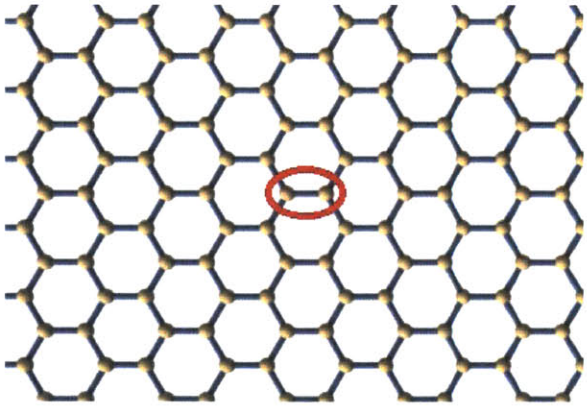

Figure 2-1: Illustration of a single layer graphene lattice. (Image courtesy of James A. Hedberg)

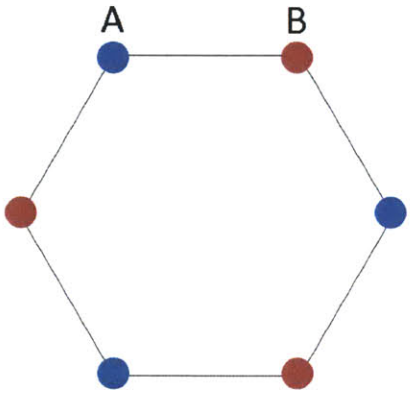

Figure 2-2: Illustration of the A and B sublattices in graphene

To understand graphene, we must first understand its lattice structure. As can be seen in Fig. 2-1, the basic periodic structure in the graphene lattice is made up of a point on the lattice and one of its nearest neighbors, circled in red. The two lattice points in each repeated structure are known as A and B sublattice sites (Fig. 2-2), and the A and B sites form two distinct sublattices within the lattice structure of graphene. If we treat the midpoint between the two lattice sites in a group as the lattice point for a new lattice, we will get another periodic lattice structure where the

repeated structure is the lattice site. This new lattice is called a hexagonal Bravais lattice (Fig. 2-3).

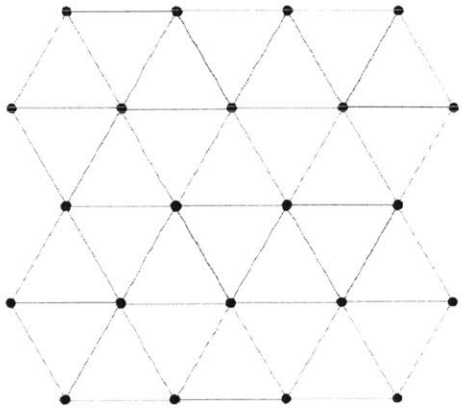

Figure 2-3: Illustration of a hexagonal Bravais lattice.

Aside from the physical lattice and the Bravais lattice, a third lattice used to describe crystalline structures is the reciprocal lattice, a lattice located in momentum space. Each lattice point $\mathbf{k}$ in the reciprocal lattice satisfies $e^{i\mathbf{k}\cdot\mathbf{R}} = 1$, where $\mathbf{R}$ is a lattice site in the Bravais lattice. Graphene, with its hexagonal Bravais lattice of lattice spacing a_R, also has a hexagonal reciprocal lattice with lattice spacing $a_k = \frac{2\pi}{a_R}$. Aside from the lattice sites, the periodic structure of a lattice can also be understood in terms of a primitive unit cell. The primitive unit cell is an area (or volume, depending on the dimensionality of the crystal) element centered around a point in the reciprocal lattice, and is the basic volumetric or area element which tiles to occupy the area of volume of the full lattice. The primitive unit cell of the reciprocal lattice is called the first Brillouin Zone, and is shown in Fig. 2-4. It is interesting to note that the structure of the reciprocal lattice depends only on the shape of the Bravais lattice, that is, it depends only on the periodicity of the crystal lattice, and not its exact structure.

2.2 Electronic Structure

Graphene is a two dimenstional crystal with a hexagonal Bravais lattice and a hexagonal reciprocal lattice. Its Brillouin Zone, due to the shape of its reciprocal lattice,

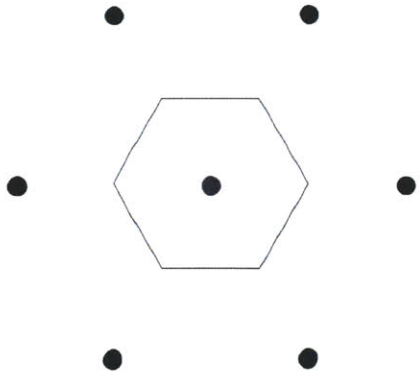

Figure 2-4: An illustration of the reciprocal lattice of graphene (black dots). The shaded region is the first Brillouin zone.

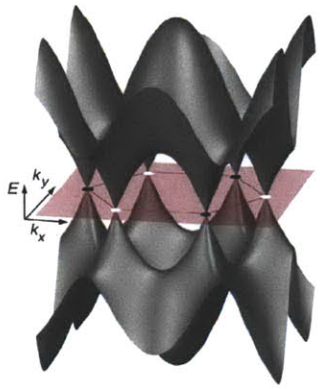

Figure 2-5: Illustration of the band structure of graphene, plotted in reciprocal space. (Illustration by C. Jozsa and B. J. van Wees)

is also a hexagon centered at a reciprocal lattice site. The basic band structure of graphene was studied by P.R. Wallace in 1947 using the a tight-binding approximation. In the tight binding approximation, electron/hole wavefunctions are taken to be linear combinations of the π orbitals localized around the lattice sites, with prefactors of $e^{i\mathbf{k}\cdot\mathbf{R}_i}$, where $\mathbf{R}_i$ is the position of the atom the orbital is localized around. The prefactors are necessary for the wavefunction to obey Bloch's theorem. By assuming nontrivial overlap between only the orbitals of nearest neighboring lattice sites, the band structure of graphene can be calculated by diagonalizing the resulting Hamiltonian [32]. The shape of the full band structure is shown in Fig. 2-5. The upper and lower bands touch at six points - the six corners of the Brillouin Zone, and the

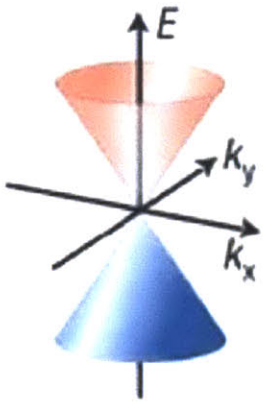

Figure 2-6: The Dirac cone, plotted as a function of $|\mathbf{k} - \mathbf{K}|$, where $\mathbf{K}$ is a corner of the Brillouin zone, vs energy. The lower cone is the valence band, and the upper the conduction band. At zero doping and no external potential applied to the graphene, the Fermi energy lies at the intersection point, $E = 0$. (Image adapted from [13])

band structure near the point is is known as the Dirac cone, shown in a closeup in Fig. 2-6. In the Dirac cone region, where the band energy is near the Fermi energy $E_F = 0$, it can be found that the energy levels obey the dispersion relation $|E - E_F| = \hbar v|\mathbf{k} - \mathbf{K}|$, where $\mathbf{K}$ is a corner of the Brillouin Zone [32]. From this dispersion relation, we can find that the group velocity of excitations (either electrons or holes) is $v_{group} = \frac{1}{\hbar}\frac{\partial E}{\partial \mathbf{k}} = v$, which is approximately $10^6 \frac{m}{s}$. The energy independence of the velocity suggest that charge carriers in graphene have an effective mass of zero. This masslessness is what gives rise to the relativistic behavior of charge carriers in graphene, only with a lower effective speed of light of $c_{eff} = 10^6 \frac{m}{s}$

Earlier, we mentioned the existence of the A and B sublattices in graphene. Each charge carrier in graphene is localized to one of these two sublattices, with some chance to go from one sublattice to another. These A and B states can be thought of as the up and down states of a spin doublet, called pseudospin. Due to the existence of this pseudospin, charge carriers in graphene will behave as massless spin-$\frac{1}{2}$ particles. They can be described via the Dirac equation for relativistic, chiral particles [5]:

$$-i\hbar v \begin{pmatrix} 0 & \partial_x - i\partial_y \\ \partial_x + i\partial_y & 0 \end{pmatrix} \begin{pmatrix} \Psi_A \\ \Psi_B \end{pmatrix} = E \begin{pmatrix} \Psi_A \\ \Psi_B \end{pmatrix} \tag{2.1}$$

where $e^{i\mathbf{K}\cdot\mathbf{r}}\Psi_A$ and $e^{i\mathbf{K}\cdot\mathbf{r}}\Psi_B$ are the wavefunctions localized to the A and B sublattices in the graphene. We can rewrite this in more concise notation as

$$v\mathbf{p}\cdot\sigma = E\psi \tag{2.2}$$

where $\mathbf{p} = -i\hbar(\frac{\partial}{\partial x}, \frac{\partial}{\partial y})$ is the two-dimensional momentum operator and $\sigma = (\sigma_x, \sigma_y, \sigma_z)$ is the vector of Pauli matrices.

Up to now, we've been considering wavefunctions in the Dirac cone centered around $\mathbf{K}$. In the opposite corner of the Brillouin Zone, in the Dirac cone $\mathbf{k} = -\mathbf{K}$, we have an second independent set of states $e^{-i\mathbf{K}\cdot\mathbf{r}}\Psi'_A(\mathbf{r})$ and $e^{-i\mathbf{K}\cdot\mathbf{r}}\Psi'_B(\mathbf{r})$ which satisfy the same Dirac equation 2.1, except with $p_x \to -p_x$. Combining these four wavefunctions into one four-component vector $\Psi = (\Psi_A, \Psi_B, -\Psi'_B, \Psi'_A)$, we see that it obeys the four-dimensional Dirac equation

$$\begin{pmatrix} v\mathbf{p}\cdot\sigma & 0 \\ 0 & v\mathbf{p}\cdot\sigma \end{pmatrix}\Psi = E\Psi \tag{2.3}$$

The three-dimensional analogue of this equation, with the two nonzero blocks having opposite signs, is the Dirac equation for massless chiral fermions. The relative signs of the two blocks correspond to left- and right-handed circular polarization. For a two dimensional system, "handedness" does not exist, as the rotation needs a third dimension to occur. Instead, the chirality of a charge carrier in graphene is tied to their direction of motion, with the two opposite chiralities corresponding to opposite momenta and thus different valleys.

Another result of the Dirac cone band structure is that current in graphene can be carried by either electrons or holes. Electrons are filled states in the conduction band, the section of the Dirac cone above the intersection point, also known as the Dirac point, and holes are empty states in the valence band, the section of the Dirac cone below the Dirac point. We can control the current carrier in graphene by changing the Fermi energy of a sample to change the carrier population in graphene, most commonly by putting a voltage on the back of the substrate the graphene is on. This

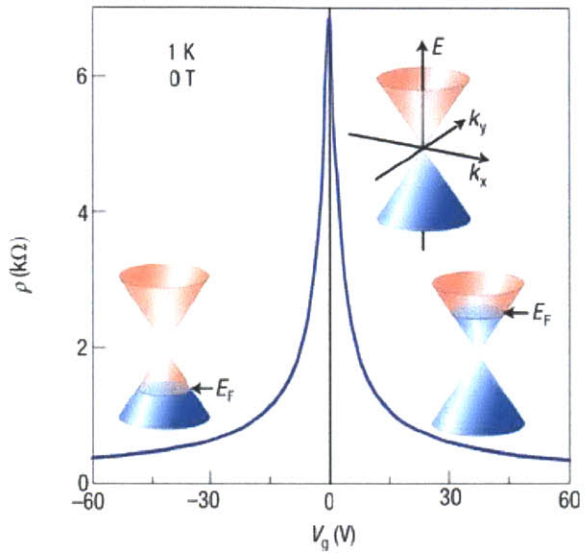

Figure 2-7: Plot showing dependence of resistance on the back gate voltage in a typical graphene device. The blue region is the occupied electronic states which fill to the Fermi energy in each Dirac cone, with the current being carried by holes for negative back gate voltages and electrons for positive back gate voltages. The large change in resistivity with the addition of few charge carriers indicate that charge carriers in graphene are highly mobile. (A. K. Geim and K. S. Novoselov 2007 [13])

is known as the back gate voltage. The further the back gate voltage is from the charge neutrality point, the more charge carriers there are in the graphene, and so the lower the resistance of the device. At the Dirac point, the resistance reaches a maximum in what is known as the Dirac peak. This dependence of conductivity/resistivity on the back gate voltage is shown in Fig. 2-7.

Surprisingly, a current can still be carried in the graphene at the Dirac point, where there should be no charge carriers. The charge is transferred via exponentially decaying modes, known as evanescent modes. In a graphene device with width much greater than its length (distance between contacts), the probability of transmission for these modes are nontrivial and obey the same equations which describe diffusive modes in a disordered metal of the same conductivity. For this reason, transport in graphene at the Dirac point is known as the pseudo-diffusive mode [30].

Chapter 3

Superconductivity and Quantum Hall Effect in Graphene

3.1 Basics of Superconductivity

The phenomena of superconductivity in normal superconductors (not high T_C superconductors) is well explained by the BCS theory of superconductivity, first proposed in the seminal 1957 paper by Bardeen, Cooper, and Schrieffer [3]. According to BCS theory, the electrons which carry charge in a superconductor will condense into pairs called "Cooper pairs" [9] at low temperatures via an attractive coupling with another electron with opposite spin via a phonon intermediary. One can understand this attraction as being caused by the charge of one electron creating deformations in the crystal lattice, resulting in regions with slightly higher density of positive charge than the rest of the lattice, which then attract the second electron and coupling the two. The phonon, as the quantum of lattice deformations, is the natural intermediary for this attractive interaction. The anti-parallel coupling of spins is selected simply due to it being more energetically favored than parallel spins. Since electrons are spin-$\frac{1}{2}$ fermions, Cooper pairs will have integral spin, and thus are bosons. At low enough temperatures, these bosons will all occupy the same ground state, with the same momentum $\mathbf{q}$ and a unique current $I(q)$. The pairing up of electrons into Cooper pairs leads to an energy gap between the ground state and the first allowable excited state.

Excitations with energies smaller than the gap, such as the scattering of electrons which causes resistance in normal conductors, are not allowed. Thus, electrons can flow freely inside the superconductor, leading to superconductivity.

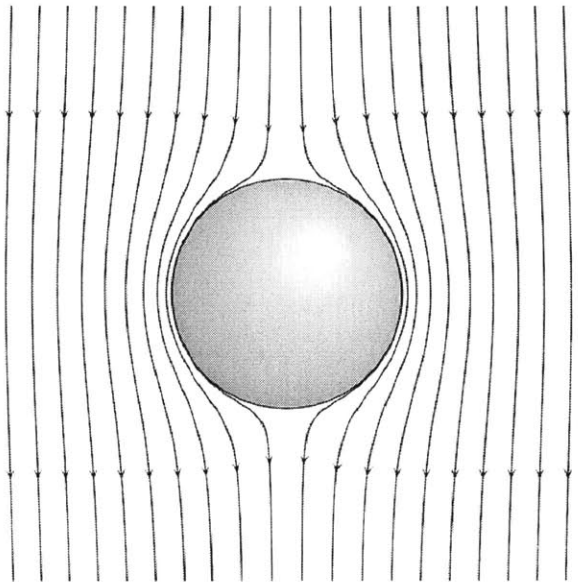

Figure 3-1: Illustration of the Meissner effect, showing the exclusion of magnetic fields from the inside of a superconductor. (Image courtesy of Geek3, commons.wikimedia.org)

The difference between a superconductor and an ideal conductor is the Meissner effect, the expulsion of magnetic fields from a superconductor when it transitions from a normal conductor to a superconductor, shown in Fig. 3-1 [21]. In a perfect conductor, the magnetic field would be constant, as any change would be counterbalanced by an induced current, whereas in a superconductor the magnetic field is always zero. Related to this is the quenching of superconductivity in a high enough magnetic field, which can be understood to be caused by the magnetic field exciting the electrons in a Cooper pair until the excitation energy is great enough to overcome the binding energy between electrons. Figure 3-2 supports this idea, as both the temperature and magnetic field contribute energy to breaking apart Cooper pairs. Because a flowing current creates a magnetic field, we can infer that there must also be a critical current which a superconductor can support, with the strength of the current depending on the material and geometry of the superconductor.

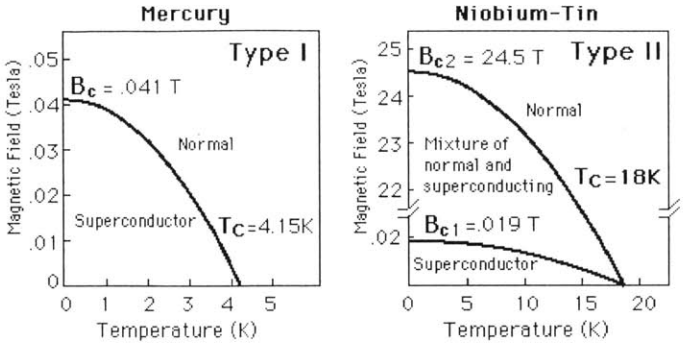

Figure 3-2: The relationship between critical magnetic field and critical temperature. Note the decrease in B_C with a rise in T_C, supporting the idea of both contributing energy to the breaking up of Cooper pairs. Note the presence of a mixed state in Type II superconductors, corresponding to magnetic vortices creating normal regions in the material. This state is not present in a Type I superconductor [28].

In type I superconductors, the magnetic field penetrates only a thin layer of depth λ, known as the penetration depth, on the surface of the superconductor, and is equal to zero elsewhere in the superconductor. In a type II superconductor, such as the niobium used in our experiments, magnetic fields are not completely excluded from the superconductors, but rather penetrate the material in cores of normal conductivity surrounded by vortices of supercurrent (Fig. 3-3). As the critical magnetic field or temperature is approached, the normal regions become more and more tightly packed, until the entire material is in the normal state. This effect helps type II superconductor remain superconducting at higher magnetic fields, at the cost of losing its full superconductivity and supporting a reduced critical current at a lower field than type I superconductors.

3.2 The Josephson Effect

Graphene itself is not a superconductor, but can carry a supercurrent when in proximity to a superconductor due to the Josephson effect, first described by Brian Josephson in 1962 [17]. When two superconductors are separated by a thin layer of another conducting material such as graphene, it is possible for Cooper pairs to tunnel through the middle layer from one superconductor to the other. This superconductor-barrier-

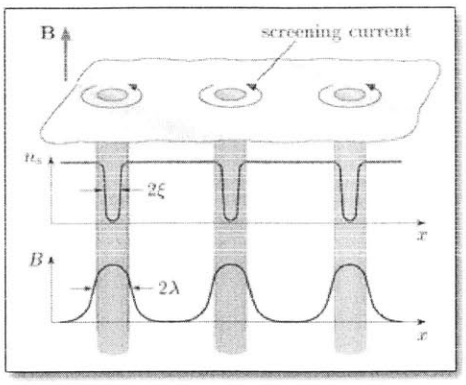

Figure 3-3: Illustration showing the penetration of a type II superconductor by magnetic fields. λ is the penetration depth in the superconductor, ξ is the coherence length of Cooper pairs in the superconductor, and n_s is the density of Cooper pairs in the material. (Image courtesy of http://openlearn.open.ac.uk)

superconductor heterostructure is known as a Josephson junction. It is important to note that a supercurrent is only sustainable while the Cooper pairs are able to propagate through the middle material with phase coherence and time reversal symmetry, since both are requirements for the existence of Cooper pairs. Luckily, graphene is capable of supporting both, and so is a suitable material for a Josephson junction. The voltage and current across a Josephson junction are given by $I = I_0 \sin(\phi)$, where ϕ is the phase difference in the wavefunction across the junction and is given by $\frac{d\phi}{dt} = \frac{2eV}{h}$ [12]. This relation gives rise to two possible effects - the DC and the AC Josephson effects.

The DC Josephson effect occurs when we put a DC voltage across the Josephson junction. When this happens, the current begins to oscillate with time as ϕ grows larger. Because of the small size of h, this oscillation is very fast and for most measurements will average out to zero. When the voltage is near zero, however, the oscillations will become slow enough to be picked up and will show up as a vertical line in a voltage vs current plot. As the voltage increases, it will finally overcome the attractive interaction between electrons in a Cooper pair, and the junction will become ohmic in its $I - V$ curve. This occurs when the voltage is equal to $\frac{2\Delta}{e}$, where Δ is the energy gap for between the superconducting and the normal conducting states. For a typical $I - V$ curve of a Josephson junction with a DC voltage bias, see

Fig. 3-4

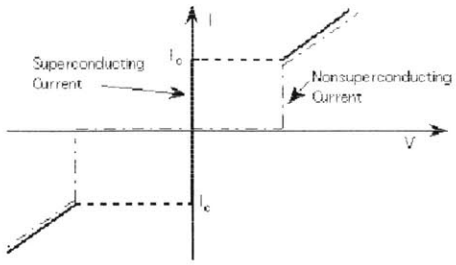

Figure 3-4: Typical $I - V$ curve for the DC Josephson effect. Note the spike in the center corresponding to a very small bias voltage. The maximum/minimum value the current reaches in this region is the maximum Josephson current I_C. As the voltage increases beyond the superconducting bandgap, the Cooper pairs' attractive interaction is broken apart and the material becomes a normal conductor with an ohmic $I - V$ characteristic. (Image courtesy A. Foster and I. E. Sayed)

If we apply an AC voltage signal on top of the DC voltage across the junction, we will see a DC component to the Josephson current when the the frequency of the DC Josephson effect oscillations is a harmonic of the applied AC frequency. Typically, these frequencies are in the GHz range, the range of microwave radiation, and so rapidly oscillating AC voltages are often achieved by applying microwaves to Josephson junctions. Experimentally, the AC Josephson effect is typically seen as steps in the $I - V$ curve of the Josephson junction (Fig. 3-5).

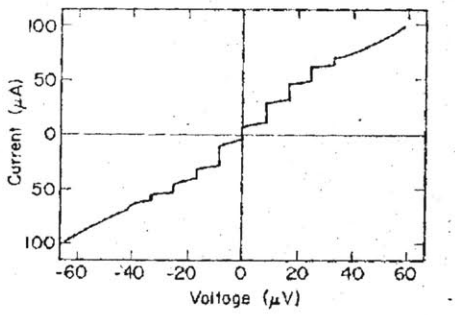

Figure 3-5: Typical $I - V$ curve for the AC Josephson effect. The steps occur when the DC Josephson frequency is a harmonic of the applied AC frequency [8].

When a perpendicular magnetic field is put across the Josephson junction, the current density along the width of the junction will differ from each other by $2\pi\frac{\phi}{\phi_0}$, where ϕ is the magnetic flux through the area between the two currents and ϕ_0 is

the flux quantum. Notice that this is identical to the situation of diffraction of light through a single slit, and thus we will observe a similar Fraunhoffer pattern emerge in the maximum Josephson current I_C, when plotted against the applied magnetic field (Fig. 3-6).

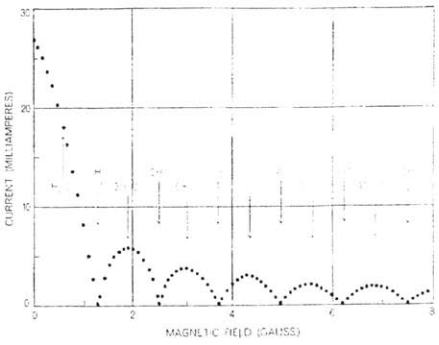

Figure 3-6: The Fraunhoffer pattern of I_C vs B. By measuring the difference in magnetic fields between succesive minima, one can find the flux quantum ϕ_0 [29].

3.3 Basics of Quantum Hall Effect

The classical Hall effect occurs when a current-carrying wire is subjected to a perpendicular magnetic field. Magnetic fields exude a force on moving charges with direction dependent on the sign of the charge, and thus will induce a separation of charges along the width of the wire. This then creates a potential difference between the top and bottom of the wire which can be measured (Fig. 3-7). The ratio of the potential difference to the applied current has units of resistance, and so is defined as the Hall resistance, $R_H = \frac{1}{n_e}$, where n is the 2D current carrier density in the wire.

In a quantum system, many classical quantities become quantized, and the Hall resistance is no exception [19]. The quantum Hall effect refers to this quantization of Hall resistance, and is caused by the quantization of electron cyclotron orbits in the material. Classically, when electrons confined to two dimensions are subjected to a magnetic field normal to their plane, they will form circular orbits known as cyclotron orbits. When the energies of this system are reduced to near zero, to the regime where quantum effects dominate, the energy of these orbits become quantized

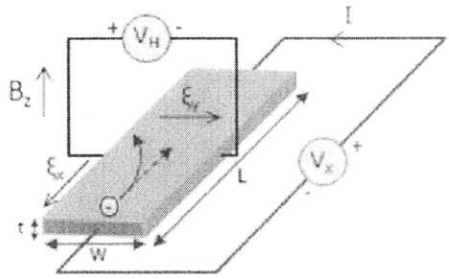

Figure 3-7: Illustration of the classical Hall effect, with electrons as the charge carriers in the circuit. Inside the slab of conductor, there is the usual potential difference across the length of the conductor as well as a Hall potential caused by the magnetic field.

into what is known as Landau levels.

To see how this occurs, consider the Hamiltonian for a system of noninteracting electrons in the $x-y$ plane, subjected to a magnetic field B in the $+z$ direction. The Hamiltonian of this system is

$$\hat{H} = \frac{1}{2m}(\hat{\mathbf{p}} - q\hat{\mathbf{A}})^2, \tag{3.1}$$

where $\hat{\mathbf{p}}$ is the canonical momentum operator $-i\hbar\nabla - \frac{q\mathbf{A}}{c}$ and $\hat{\mathbf{A}}$ is the vector potential generating the magnetic field. By choosing the Landau gauge, with $\mathbf{A} = (0, Bx, 0)$, and taking the y component of the wave function to be a plane wave so the the wavefunction has the form $\psi(\mathbf{r}) = e^{ik_y}\phi(x)$, we can rewrite the Hamiltonian as

$$\hat{H} = \frac{\hat{p_x}}{2m} + \frac{1}{2}m\omega_c^2\left(\hat{x} - \frac{\hbar k_y}{m\omega_c}\right)^2, \tag{3.2}$$

with $\omega_c = \frac{qB}{mc}$. This is simply the 1D harmonic oscillator Hamiltonian, with the center of the oscillator at $x_0 = \frac{\hbar k_y}{m\omega_c}$, and so its energy levels are quantized at $E = \hbar\omega_c(n + \frac{1}{2})$ (see Fig. 3-8). If we consider a system of finite size, then the number of possible states is limited by the number of k_y's. k_y must satisfy the plane wave periodic boundary condition $k_y = \frac{2\pi N}{l_y}$, where l_y is the dimension of the system in the y direction. We also know that x_0 must be between 0 and l_x, so we see that the degeneracy of each system is $(2S+1)\frac{m\omega_c l_x l_y}{2\pi\hbar}$, where S is the spin of the charge

carriers. Letting $Z = qe$, we can rewrite this as $Z\frac{\phi}{\phi_0}$, where $\phi = Bl_x l_y$ is the magentic flux through the system and $\phi_0 = \frac{hc}{e}$ is the flux quantum.

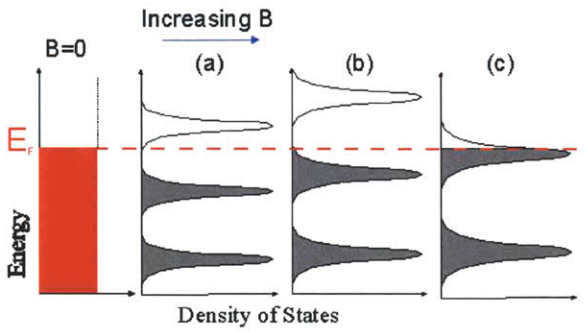

Figure 3-8: Landau levels at various magnetic fields. Due to disorder and impurities in all samples, the energies of the Landau levels become broadened from the ideal zero width peaks. (Image courtesy of D. R. Leadley).

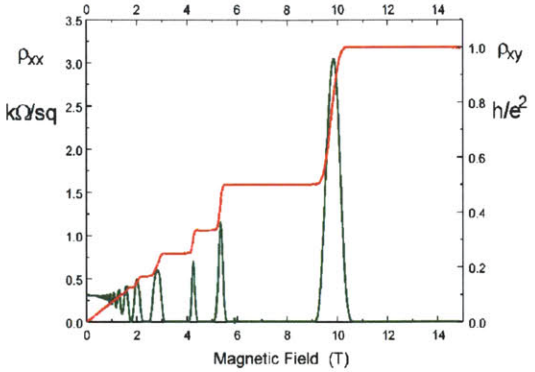

Figure 3-9: Resistivity of a a quantum Hall system as a function of the perpendicular magnetic field through it. The red curve shows the plateaus in the Hall resistance, and the green curve shows the peaks in longitudinal resistivity. (Image courtesy of D. R. Leadley).

How does this effect lead to the quantization of Hall resistance? For each Landau level beneath the Fermi level, we have an additional $\frac{eB}{hc}$ current carriers per unit area. This density only changes as another Landau level cross the Fermi energy, either by changing the Fermi energy of the system or the Landau levels by altering the magnetic field. Since the Hall resistance depends on the density of charge carriers, it can only change by multiples of $\frac{e^2}{h}$. Between these Landau level crossings, the Hall resistance remains unchanged in what is known as plateaus. Similarly, the resistance in the direction of current flow also depends on the so-called filling factor, or how many Landau levels are below the Fermi energy and thus filled. When the Fermi level is between two Landau levels, there are no states available for electrons to scatter into, and so current flows without resistance (Fig. 3-9). Normal resistance is restored when the Fermi energy is near a Landau level, such that there is are unfilled states near the Fermi energy that charge carriers can scatter into.

When the Fermi energy is between two Landau levels, current in a quantum Hall material is carried through edge states. These edge states arise because near

the edge, the energy of Landau levels will rise to infinity so that electrons remain confined in the material (Fig. 3-10). This rising energy will eventually meet the Fermi level, creating states at the edge of the material with only 1 dimension along the edge. When the Fermi level is between Landau levels in the bulk of the material, there are no free electrons which can conduct, only localized states, in the bulk. These states are localized because for any system, there are impurities which create potential wells in the material, localizing Landau states in the bulk and preventing them from conducting. At the edge where the Landau level meets the Fermi energy, however, electron states occupy the entire edge of the system, and thus are available for conduction. The more Landau levels are below the Fermi energy, the more 1D channels are available for conduction, giving another explanation to the quantization of resistance in a quantum Hall system.

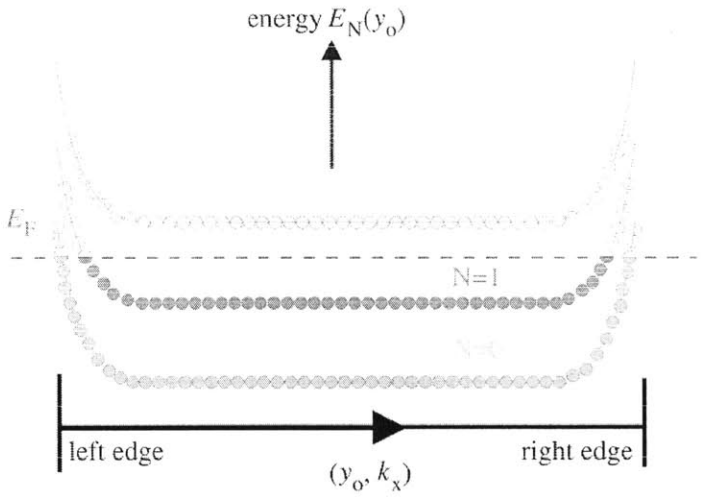

Figure 3-10: Ideal Landau levels in a finite material. The Landau levels must rise to infinity so that charge carriers remain inside the material, and where occupied Landau levels meet the Fermi energy, 1D conducting edge states are formed [31].

3.4 Quantum Hall Effect in Graphene

Graphene's unique electronic structure results in it having not a normal quantum Hall effect, but what is known as a half-integer quantum Hall effect [24]. This is caused by the fact that the first Landau level at $E = 0$ only has half the degeneracy of the

other Landau levels due to the charge carriers being massless Dirac fermions. Thus, the first Landau level only needs half the usual number of carriers, be they electrons or holes, to fill up. The rest of the levels have the usual degeneracy, and so the Hall resistance in graphene is quantized with the same difference between plateaus, with the only difference being that they have resistances of $(n + \frac{1}{2})\frac{e^2}{h}$ instead of $n\frac{e^2}{h}$ (Fig. 3-11).

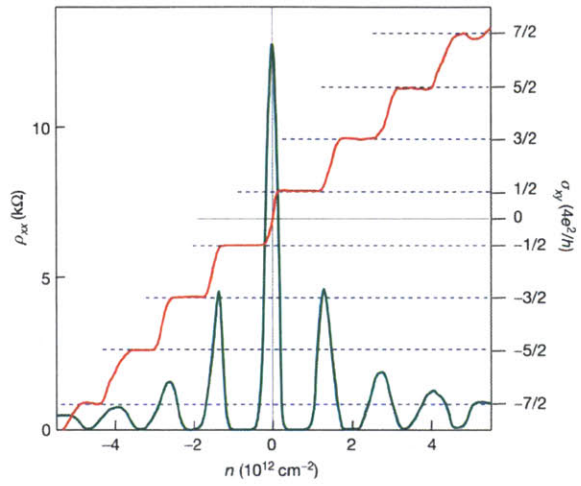

Figure 3-11: Hall conductivity (in red) and longitudinal resistivity (in green) for a single layer graphene system [24].

Another result of the relativistic nature of the charge carriers in graphene is that the edge states which carry the current in a quantum Hall system can be chiral - currents are spin polarized, and currents traveling opposite directions have spins polarized in opposite directions [1]. To understand how this occurs, see Fig. 3-12. The blue and red curves are the Landau levels which have been split due to Zeeman interactions between the magnetic field and the spin of the charge carriers. The zeroth Landau level is occupied by both holes and electrons, so near the edge the energy curves both up and down to contain holes and electrons. When the Fermi energy is between the spin up and spin down levels of the zeroth Landau level, two edge states are created - the upwards curving spin down level and the downwards curving spin up level. These two edge states will travel in opposite directions, since their velcity $v = \frac{d\epsilon}{dk}$ are opposites, and they contain oppositely-oriented spins. In this manner, the zeroth Landau level edge states are chiral.

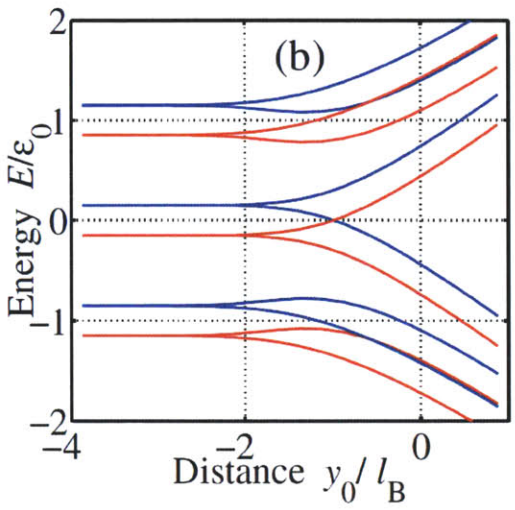

Figure 3-12: Energy of Landau levels in graphene near the edge. The states curving downward are the energy levels for electrons, and the states curving upward are the energy levels for holes [1].

3.5 Superconductivity in Graphene

As discussed before, graphene itself is not a superconducting material, but takes on superconducting characteristics when contacted with superconductors due to the Josephson effect. This effect was first observed by Heersche et al in 2007 [15], and exhibits several remarkable properties.

The first of these properties can be seen in the effect of back gate voltage on the supercurrent in a graphene Josephson junction. There is a supercurrent no matter if the current carrier in graphene is electrons or holes, and is symmetric about the Dirac point (Fig. 3-13). This indicates that supercurrents in graphene are carried by both electron and hole Cooper pairs. Even in the pseudo-diffusive mode, we can see that electronic transport in graphene is phase-coherent and obeys time-reversal symmetry.

The second property is related to the fact that the two electrons/holes in Cooper pairs are time-reversed states, having opposite momentum and spin. For a low-energy charge carrier with momentum $\mathbf{k}$ in the phase space, its time-reversed state, with momentum $-\mathbf{k}$, occupies the opposite corner of the Brillouin zone. These two phases occupy different valleys, and so have opposite chiralities. Through this, we see that contact with a superconductor phase coherently couples the two valley states in

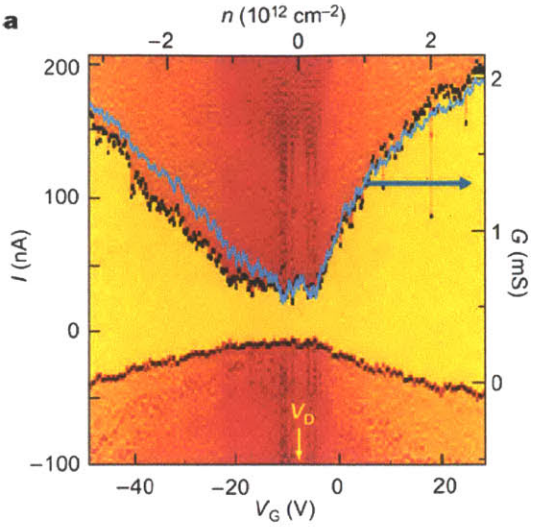

Figure 3-13: The supercurrent in a graphene Josephson junction as a function of the back gate voltage. The color scale is the differential resistance $\frac{dV}{dI}$ across the junction, with yellow indicating 0 - superconducting region. Note that the supercurrent is nearly symmetrical about the Dirac point, and so is carried by Cooper pairs of holes and electrons in the negative and positive back gate voltage regions, respectively [15].

graphene which are otherwise decoupled. Thus, the dynamics of this superconducting graphene system must be described by the full two-valley, time reversal symmetric Hamiltonian - Eq. 2.3.

3.5.1 Andreev Reflections

The next property is known as Andreev reflection [4], and has several aspects. Andreev reflection occurs when a low-energy electron (energy ϵ less than superconducting gap V_G) from a normal conductor meets the interface between the normal conductor and a superconductor. Since electrons with energy below the superconducting gap must exist in pairs in superconductors, another electron must enter the superconductor that is a time-reversed version of the entering electron, so that these two electrons can propagate in the superconductors as Cooper pairs. This extra electron leaving causes a hole to be created in the normal conductor with energy $E_F - \epsilon$. When the electron and hole states both lie in the conduction band, conservation of momentum then requires that the hole be traveling in the opposite direction as the incident

electron.

In normal metals, excited states are at an energy much higher than the level of the valence band compared to the superconducting band gap, and so they only exhibit Andreev retro-flection. In graphene, however, it is possible for the electron to belong to the conduction band and the hole from the valence band due to the unique contact between the valence and conduction bands at the Dirac point. By gating the graphene so that the Fermi energy is at the Dirac point, any electron excitation will be turned into a hole excitation in the valence band.

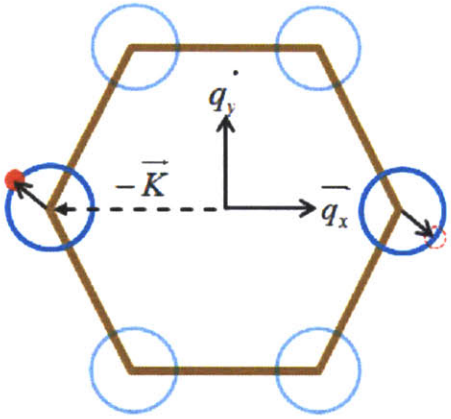

Figure 3-14: The locations of the incident electron in the $-\mathbf{K}$ valley (solid circle) and reflected hole in the $\mathbf{K}$ valley (hollow circle) with respect to the Brillouin zone. (Image courtesy of Joel Wang).

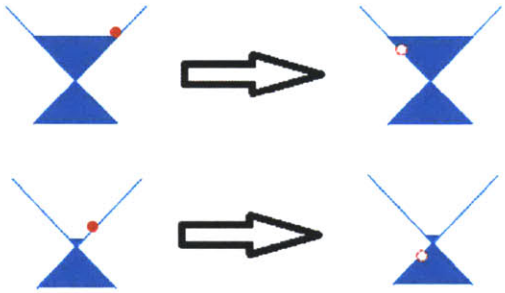

Figure 3-15: The locations of the incident electron and reflected hole in the Dirac cone. Note the different slopes in the regions occupied by the reflected hole in the conduction band (top figure) and the valence band (bottom figure). (Image courtesy of Joel Wang).

To analyze the situation, let us consider a graphene-superconductor system where the superconductor occupies the region $x < 0$ and the graphene $x > 0$, with the interface at $x = 0$. Consider then the excitation energy of a charge carrier at the graphene-superconductor boundary: $\epsilon = |E - E_F| = |E_F \pm \hbar v(k_x^2 + k_y^2)^{1/2}|$, where the $(+)$ and $(-)$ signs are excitations in the conduction and valence band, respectively. k_y and ϵ are conserved at the reflection. In addition, the velocity in the x direction, $v_x = \frac{1}{hbar}\frac{d\epsilon}{dk_x}$, must be positive for a reflected solution. As mentioned earlier, the reflected hole will be an empty state at energy $E_F - \epsilon$. Thus, the reflected hole will be in the conduction band when the energy ϵ of the incident electron is less than the

Fermi energy E_F, and is in the valence band when ϵ is greater than E_F. A hole in the conduction band, as shown in Fig. 3-15, has a slope $\frac{d\epsilon}{dk_x}$ opposite of the slope of the incident electron. The hole will have both v_x and v_y opposite the incident electron and is a retro-reflected hole. A hole in the valence band, in contrast, has a slope $\frac{d\epsilon}{dk_x}$ that is equal to the incident electron. The hole will have v_x opposite the incident electron, and v_y equal to that of the incident electron, resulting in specular Andreev reflection.

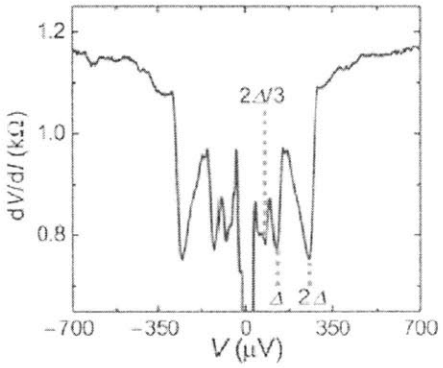

Figure 3-16: Differential resistance plotted against bias voltage across a graphene Josephson junction. The indicated peaks in the differential dips in the differential resistance are signatures of multiple Andreev reflection [15]

Aside from specular Andreev reflection, Josephson junctions, including SGS Josephson junctions, will exhibit multiple Andreev reflection (MAR). This effect can be seen as dips in the differential resistance when the bias voltage is twice the superconducting gap Δ divided by an integer. In Fig. 3-16, one can observe three dips, occuring at $V = \frac{2\Delta}{3}$, $V = \frac{2\Delta}{2}$, and $V = 2\Delta$, where $\Delta = 0.125\,mV$ is the superconducting gap of the Ti/Al bilayer used in the device. To see how this happens, consider a Josephson junction with bias voltage eV. The probability of Andreev retroflection as a function of incident particle energy at the two contacts are shown in Fig. 3-17. For an electron from S_L incident on S_R with energy in the lowest energy shaded region, a retroreflected hole would be created with energy in the second shaded region and would travel back to S_L, where it would be reflected again as an electron back to S_R with energy in the third shaded region. Thus, some of the charge carriers in the graphene, specifically those with energies in the lower shaded regions, actually create

extra charge carriers through Andreev retroflection. This process is called multiple Andreev reflection.

The conductivity of the graphene, due to this increase in the charge carrier density, would increase. For a bias voltage between $\frac{2\Delta}{n}$ and $\frac{2\Delta}{n-1}$, there would be $n+1$ shaded regions. As the bias voltage is lowered, the size of the shaded region would shrink, decreasing the conductivity, until eV is low enough that it goes from above $\frac{2\Delta}{n}$ to below. There would then be one more shaded region, indicating another allowed reflection and an increase in the number of extra charge carriers created by a multiply reflected charge carrier and so a sharp increase in the conductivity which then starts to decrease again. This cycle of increasing and decreasing conductivities leads to the series of dips in the differential resistance seen in a superconducting sample. Because MAR can only occur in a superconductor-normal conductor interface through which Cooper pairs can tunnel, it can be used as an indication of the presence of proximity-induced superconductivity in a graphene Josephson junction.

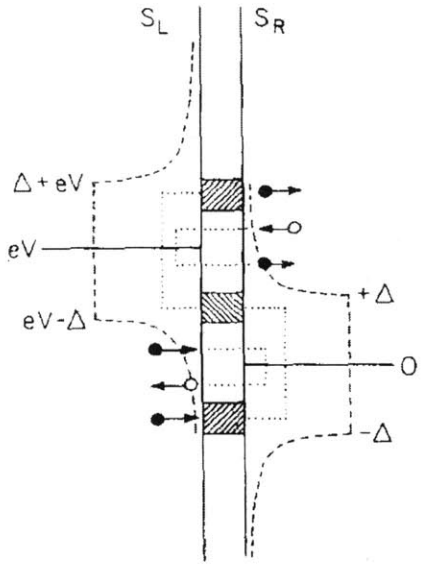

Figure 3-17: Probability of Andreev retroflection (dotted line) as a function of incident particle energy at the two gaps, with the probability reaching unity between $E = \Delta + eV$ and $\Delta - eV$ on the left side and between $E = +\Delta$ and $E = -\Delta$ on the right side. [18]

Chapter 4

Device fabrication

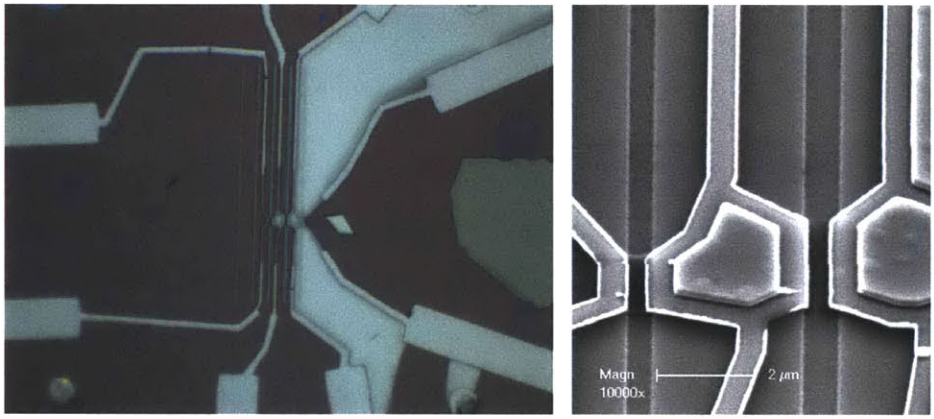

Figure 4-1: Images of a suspended graphene Josephson junction on SiO_2 substrate with niobium leads, taken with optical (left) and scanning electron (right) microscopes. In the SEM image, the dark areas between the metallic leads are regions of suspended graphene.

In this experiment, we wish to observe the transport properties of Josephson junctions in the quantum Hall regime. For this to be possible, we must have graphene in the quantum Hall regime, which requires large magnetic fields. However, we also need superconducting leads, which places an upper bound on the strength of magnetic field we can use. In order to minimize the magnetic fields needed to observe quantum Hall effects in graphene, we need high mobility samples. There are two methods commonly used to achieve high mobility graphene samples - suspended graphene [7] and graphene on hexagonal boron nitride (hBN) [10]. Both of these methods work

by separating the graphene from the nonuniform surface on a substrate like SiO_2, whose surfaces contain impurities and trapped charges and can create potential wells and peaks which can scatter charge carriers in graphene and thus reduce the mobility of the sample. This thesis will present the fabrication process we have developed to produce Josephson junctions build with suspended graphene samples.

4.1 Basics of Graphene Exfoliation

Graphene is normally produced with two different methods - chemical vapor deposition (CVD) and exfoliation. CVD graphene is made by flowing gas containing carbon across a high temperature substrate, such as copper. Carbon atoms will then slowly arrange themselves into a crystal lattice on top of the substrate, and by controlling the growth rate through temperature and other paramters, graphene can be grown with high uniformity. Exfoliated graphene, in contrast, is made by placing bulk samples of high quality graphite, such as kish graphite which is precipitated from molten iron, into contact with a substrate. The adhesive forces between the graphite and substrate may in some cases be great enough to peel slayers of graphene off of the bulk sample. Because of the low probability of only a single layer of grpahene being peeled off in this process, the traditional method for exfoliation has been to use a tape covered with graphite to contact the substrate (Fig. 4-2), so that a reasonable number of graphene flakes can be exfoliated.

While exfoliated graphene is of very high quality, being nearly ideal crystals, it is difficult to produce in large quantities, and the placement of the graphene on the substrate is uncontrollable by the exfoliater. The control of graphene placement is especially important in our experiment, as we need to be able to precisely place graphene flakes onto etched trenches in the substrate.

To resolve this problem, instead of exfoliating graphene directly on top of the SiO_2 substrate we want to build our devices on, we deposit graphene onto a film of Poly(methyl methacrylate) (PMMA), and then use a flip-chip bonder (Fig. 4-3 to transfer the graphene from the PMMA film to the substrate. The flip-chip bonder

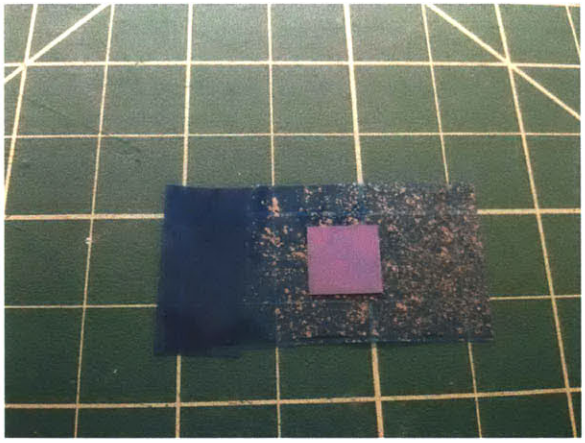

Figure 4-2: Graphite-covered tape and the substrate on which the graphene is to be exfoliated. The graphite is made to cover the blue tape, and then stuck to the substrate and removed, leaving behind graphene. For reference, the grid shown is 0.5 in. $\times$ 0.5 in.

has a micron-scale precision, which is the precision needed in order to place graphene accurately onto $10 - 15$ micron sized sets of trenches in our SiO_2 substrate.

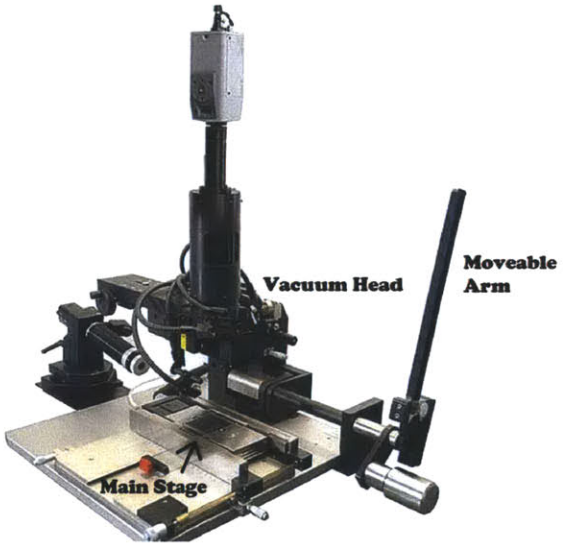

Figure 4-3: The flip-chip bonder used to place graphene flakes onto trenches etched into the substrate (Image courtesy of Finetech GmbH & Co. KG)

4.2 Substrate Preparation

The first step in our fabrication process is the preparation of substrates to which we will transfer graphene.

To produce trenches for suspended graphene devices, we pattern the desired geometry for our trenches onto substrates coated with PMMA resist using electron beam lithography. Once the pattern is developed, the trenches are etched into the substrate using reactive-ion etching, with the results shown in Fig. 4-4. The trenches are approximately 150 nm deep, with a rectangular profile so that the graphene will not cling on to the sides of the trench and will instead become suspended.

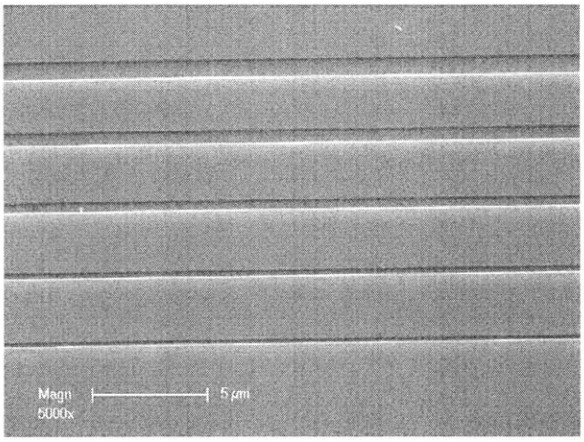

Figure 4-4: SEM image of a typical system of trenches. The trenches shown have a depth of 150 nm

4.3 Graphene Deposition

After the substrate is prepared, we must prepare the graphene flakes for transfer. For an illustration of this preparation process, see Fig. 4-5. The first step in our preparation is to spin polyvinyl alcohol (PVA) and then PMMA onto a large Si chip, and lightly bake the resist so it will retain its shape after being removed from the substrate. The PVA is used because it does not adhere as strongly to the substrate as PMMA, and so the PMMA+PVA film can be easily detached from the substrate. Next, we place a piece of tape with a window cut out on top of the PMMA. This tape

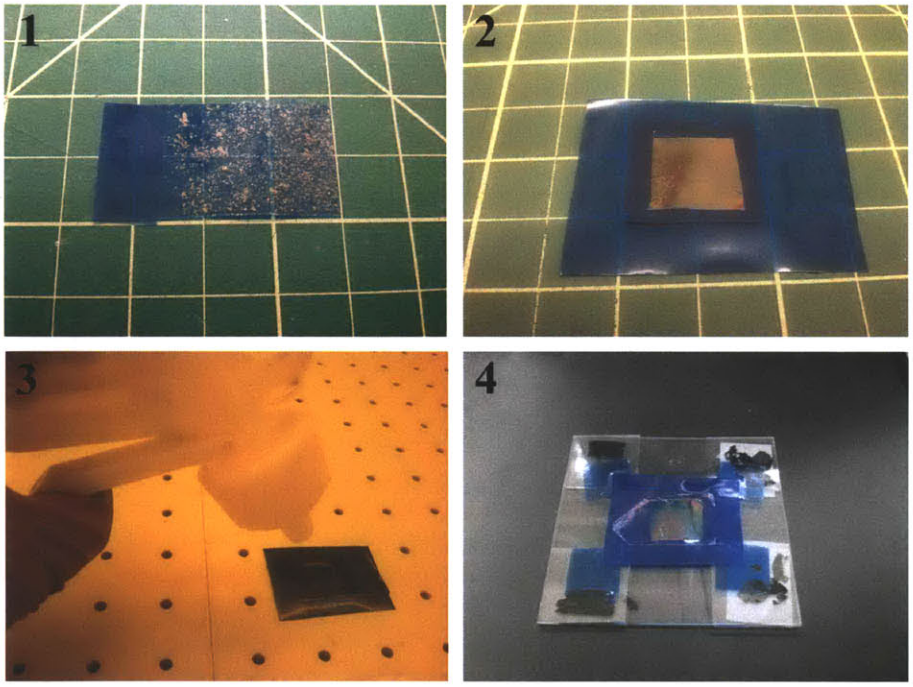

Figure 4-5: Series illustrating the graphene deposition process. Picture 1 shows the tape used to deposit graphene onto PMMA. Picture 2 shows the PMMA with tape acting as a window. Picture 3 shows deposition of graphene onto PMMA, with a nitrogen gun providing the pressure. Picture 4 shows PMMA film mounted onto a glass slide frame.

will serve as the support structure for our free standing PMMA film. After the film is prepared, we will deposit graphene onto the surface of the PMMA film using the traditional tape method. The tape containing PMMA with graphene is then lifted off from the substrate and mounted onto a support frame.

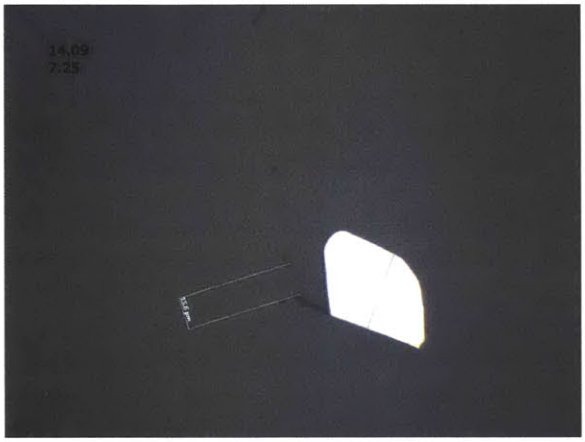

Figure 4-6: Graphene on PMMA seen through an optical microscope, with the PMMA between the graphene flake and the microscope objective. The white region is a thick graphite flake, most likely more than 5-10 layers thick. The lightest region between the white measurement lines is a single layer graphene flake, and the darker region is 3-4 layers thick.

The film is mounted so that the side with graphene on it faces down, both to better protect the graphene from dust and other impurities and because in this configuration it is easier to see graphene under an optical microscope. After the graphene is deposited and the PMMA film mounted, single layer graphene flakes are located using a high power optical microscope (Fig. 4-6). Once that is done, washers are placed on the surface of the PMMA facing up, so that the graphene flake is near the center of the area inside the washer. These washers will maintain tension in the PMMA film during transfer, as it is necessary for the PMMA to remain flat during transfer to ensure the required transfer precision. Lastly, a final layer of tape is placed on top of the washer so that the flip-chip bonder has a rigid surface to attach to.

4.4 Graphene Transfer

The key step in our fabrication process is the transfer of graphene flakes from a PMMA film to the desired substrate. To do this, we use a flip chip bonder, normally used to bond two semiconductor chip components to each other or a semiconductor component to external circuitry. A flip chip bonder first uses a vacuum attached to a moveable arm to grab on to the back of a small semiconductor chip. Next, the component which the chip is to be bonded to is fixed via vacuum to the main stage. Using a semi-transparent mirror, the position of the stage can be adjusted so that when the arm is moved back down, the small chip will land on the desired location of the component on the main stage. The stage can then heats the components up so that the contacts on the two pieces are bonded to each other.

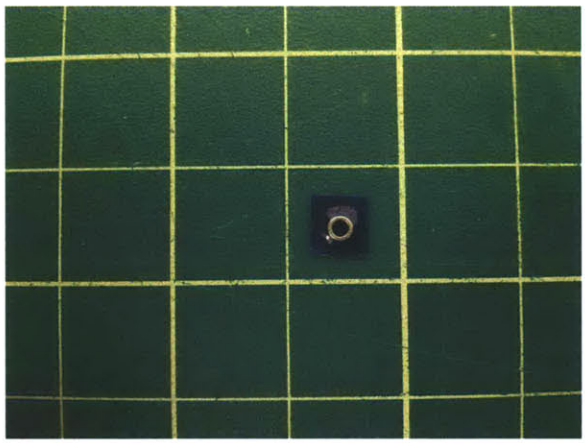

Figure 4-7: Picture of the washer after it's been cut away from the rest of the film and ready for transfer. The moveable arm will grab onto the tape on the back of the washer, and transfer the graphene which is currently on the side of the PMMA facing the reader onto our prepared substrate.

In our case, however, we use bonder to "bond" PMMA with graphene flakes onto a SiO_2 substrate. To begin the transfer process, we separate a small region of the PMMA around a desired washer so that it can be placed onto the moveable arm of the flip chip bonder (Fig. 4-7). The substrate to be transferred onto is then fixed onto the stage, and positioned so that the graphene flake will land on the desired location on the substrate, which can usually be done within $1-2\,\mu$m. Once the stage is ready for transfer, it is heated up. The heating of the substrate is necessary for the PMMA

and graphene to adhere to the substrate, and also causes the PMMA film to expand and flatten when it comes into contact with the substrate, flattening the graphene further after the transfer and improving the quality of the transferred flake.

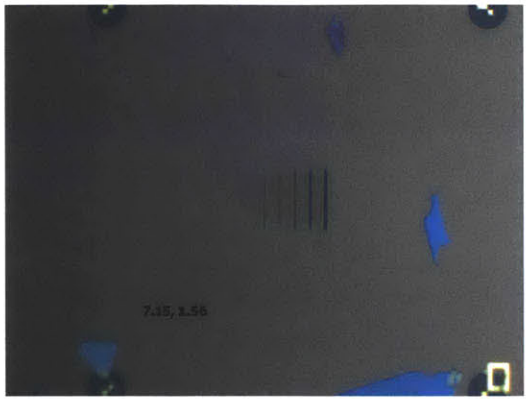

Figure 4-8: Optical image of graphene (pink) after it has been transferred onto a set of trenches (blue). The light pink region is single layer graphene, and the darker pink region is bilayer graphene.

4.5 Graphene Annealing

To create our graphene Josephson junctions, we write patterns for the leads in PMMA resist using electron beam lithography, and then sputter niobium metal to form leads. There is a thin layer of titanium between the niobium and the graphene which acts as a wetting layer, and is necessary to make the metal-graphene interface transparent enough to electrons that Cooper pairs can tunnel through the interface and into graphene.

The first step in the lithography process is the preparation of our transferred graphene for lithography. Due to the delicate nature of Josephson junctions, they cannot be cleaned with the usual methods of heat annealing, during which the device is subjected to high temperatures in an oven to remove the impurities from the surface of the graphene, or current annealing, which heats the graphene using resistive heating [23]. To avoid annealing after the devices are finished, we must clean the graphene surface before the lithography step. After the cleaning, a thin layer of Al_2O_3 will be deposited on top of the graphene to protect it from further contamination by the

PMMA resist.

For a graphene flake suspended over trenches, the heat annealing process creates ripples on the graphene surface [2]. These ripples can scatter charge carriers in the graphene, resulting in lower mobility, and thus must be avoided. Currently, we have two solutions to this problem. The first is to current anneal the sample after transfer. Current annealing has proved to be useful for annealing the graphene into high mobility devices 5.1 without creating ripples. To do this, we use the PMMA used in transfer as a resist and write current annealing leads using electron beam lithography, develop the patterns, and evaporate Cr/Au leads onto the substrate. Through these leads, shown in Fig. 4-9, we will pass the current into and anneal the graphene. A second method we are currently exploring is to fill the trenches with ALD (atomic layer deposition) Al_2O_3 before transfering, so that after transfer the graphene is no longer suspended. We use ALD instead of evaporated oxide because ALD Al_2O_3 has a flatter surface than evaporated Al_2O_3, so that the transferred graphene will be flat after the oxide is removed. Then we can heat anneal the graphene as usual, and the oxide can be removed at the same time as the protective layer of aluminum oxide used later in the fabrication process.

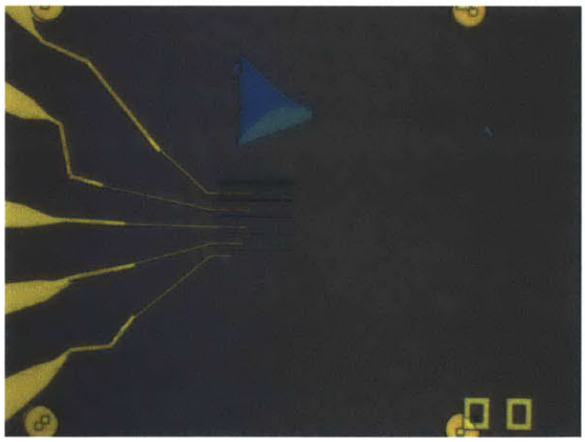

Figure 4-9: Cr/Au leads used to current anneal the graphene in preparation for lithography

Following cleaning of the graphene samples, a 5 nm layer of Al_2O_3 is evaporated onto the surface of the graphene to protect the surface of graphene from further contamination. After the evaporation, a trilayer PMMA structure is spun on top

of the hBN graphene and transferred on top of graphene over trenches as a positive resist for electron beam lithography in the next step. The need to transfer instead of spin PMMA is because suspended graphene rolls up and becomes unusable after PMMA is spun on it. The structure of the trilayer graphene is shown in Fig. 4-10.

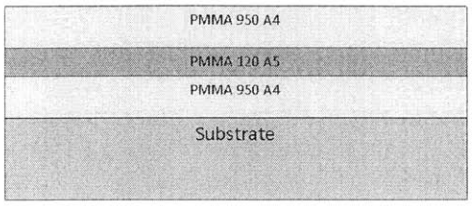

Figure 4-10: Structure of the trilayer PMMA used as resist for e-beam lithography. The structure is made of a layer of PMMA 120 A5 sandwiched between two layers of PMMA 950 A4, and has a total thickness of $\approx 450\ nm$. The purpose of the trilayer structure is to facilitate liftoff.

4.6 Lithography, Development, and Deposition of Leads

After the PMMA has been spun, we pattern the metallic leads for our devices with a Raith 150 electron beam lithography machine. The resulting pattern is developed, and since PMMA is a positive resist, the portions of the resist which has been written on with an e-beam is more soluble, and dissolves away leaving the underlying material exposed. Next, the sample is immersed in TMAH, a highly selective etchant for Al_2O_3, for a short time, so that the oxide covering the developed region of the PMMA will dissolve away and the graphene can be contacted by metal. The oxide between the remaining PMMA and graphene is not etched away due to the short immersion, and still protects the graphene from PMMA contamination. The development is done at low temperatures, using a cold-development process [26] [16] to achieve the resolution necessary to create devices at the 500 nm scale.

After development, the substrate is placed into an AJA ATC sputtering system at

ultra high vacuum ($\approx 10^{-}9$ torr). The UHV is necessary to reduce the amount of titanium oxide which forms during the sputtering process, as it reduces the transparency of the metal-graphene interface and could even prevent the tunneling of Cooper pairs altogether. After the sample has been sputtered, the PMMA and excess metal whic has been sputtered onto the undeveloped PMMA are lifted off via submersion in hot acetone. It is at this stage that the trilayer PMMA is necessary. Unlike evaporation, in which metal is deposited onto the surface from the top, in sputtering the metal is deposited onto the surface with a spread of incident angles. With a single layer of PMMA resist, the developed structure has a uniform width, and so the sputtered metal covers the entire surface (Fig. 4-11) and makes it impossible for the acetone to penetrate to the resist and remove the excess metal. The PMMA 120 A5 is more sensitive to exposure, resulting in an undercut profile in the developed PMMA, as shown in Fig. 4-12. With the undercut, the acetone can reach the resist and dissolve it away, taking the excess metal with it.

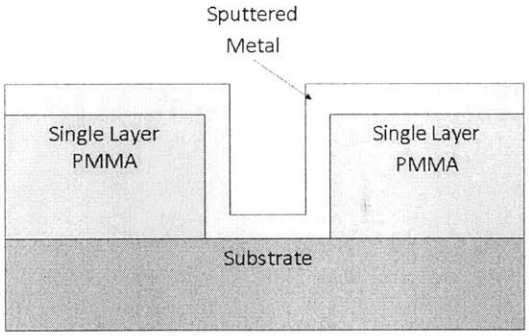

Figure 4-11: Developed single layer PMMA resist. Note how the metal covers the entire inside surface of the developed region, resulting in the acetone being unable to reach the resist and the excess metal remaining on the substrate.

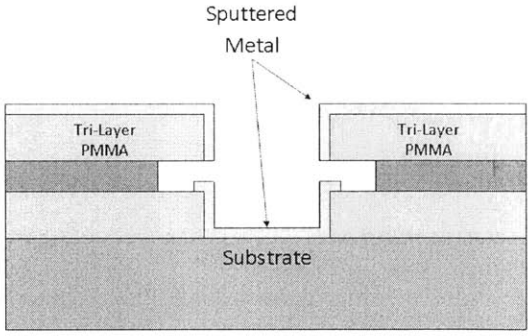

Figure 4-12: Developed trilayer PMMA resist, with an undercut in the 120 A5 layer. Note how there is a gap in the metal for the acetone to reach the resist and dissolve it.

Following the liftoff, the sample is again dipped into TMAH to remove the remaining Al_2O_3. A suspended sample must be dried after a brief immersion in hot 2-propanol (isopropyl alcohol) at 90° C, as the low surface tension of hot IPA ensures that the graphene flake is not pulled to the bottom of the trench by the surface

tension of the liquid during the drying process and remains suspended after drying.

Chapter 5

Measurements and Data

Our primary method of studying suspended Josephson junctions is via transport measurements. By measuring the resistance, conductivity, and size of the supercurrent as a function of the magnetic field and gate voltage, we can infer the behavior of electrons, holes, and Cooper pairs in graphene while it is in the quantum Hall regime.

The measurements presented here were taken at 4 K, with the devices dipped into liquid He_4 inside a dewar. See Fig. 5-1 for an image of the insert on which the chips are mounted.

5.1 Basic Characterization of Flake Quality

The quality of the graphene flake is determined by two factors - its doping level and mobility. Both of these two factors can be qualitatively analyzed by measuring the resistance of the graphene as a function of back gate voltage. Ideal graphene is most resistive at zero gate voltage, as there are no free charge carriers in the graphene at that point. However, impurities in and on the graphene can introduce charge carriers into the system, be they positive or negative charges, into the graphene, resulting in the Dirac peak occuring at a gate voltage other than zero. Consequently, the closer the Dirac peak is to zero, the less impurities there are in and on the graphene.

In this measurement, the back gate voltage is applied via a voltage source connected to the chip carrier, which is electrically contacted to the Si substrate via a

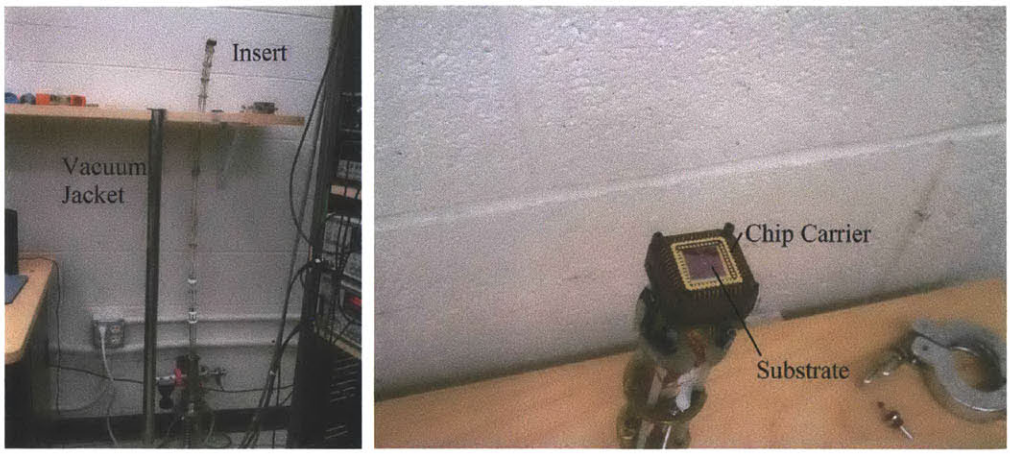

Figure 5-1: Insert on which the substrate and chip carrier is mounted and dipped into liquid He_4 to make 4 K measurements.

conducting adhesive. To measure the resistance, we apply an AC current across the junction of interest and measure the voltage across the junction using a lock-in amplifier. The lock-in amplifier outputs a signal with a specified frequency, in our case chosen to minimize the interference from outside signals, and then filters out all the input signals it receives except the one with the same frequency as the output. In this way, only the voltage caused by our input AC current will be measured by the lock-in, and interference from sources such as the 60 Hz noise from nearby power lines.

The mobility of charge carriers in a rectangular flake of graphene is given by the equation $\frac{1}{C_G}\frac{\partial\sigma}{\partial V_G}$, where C_G is the capacitance between the graphene and the back gate, σ is the conductance of the sample, and V_G is the applied back gate voltage. The number of interest is the highest value of mobility over the range of back gate voltages, which should ideally occur on the two sides of the Dirac peak where the conductivity increases dramatically away from the Dirac point. High mobility devices are needed to study the properties of charge carriers in graphene and their interactions. In a low mobility sample, the transport properties are dominated by the scattering of charge carriers off of trapped charges and impurities on the graphene instead of the intrinsic properties of the charge carriers in graphene. Typically high values for mobility are around $200,000\,cm^2\,V^{-1}\,s^{-1}$, at which point one can observe ballistic tranport of

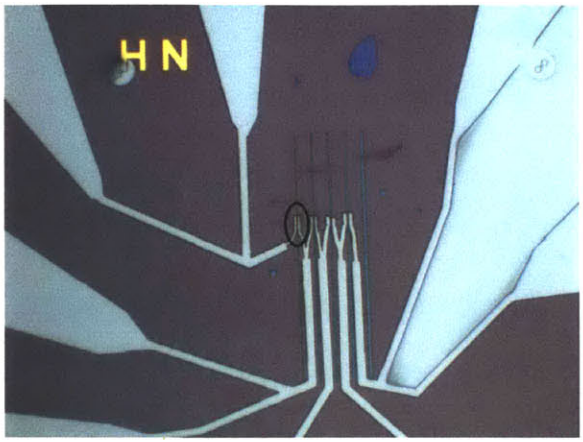

Figure 5-2: Suspended graphene Josephson junction device which underwent no annealing before measurement. The junction measured is the leftmost one (circled in black)

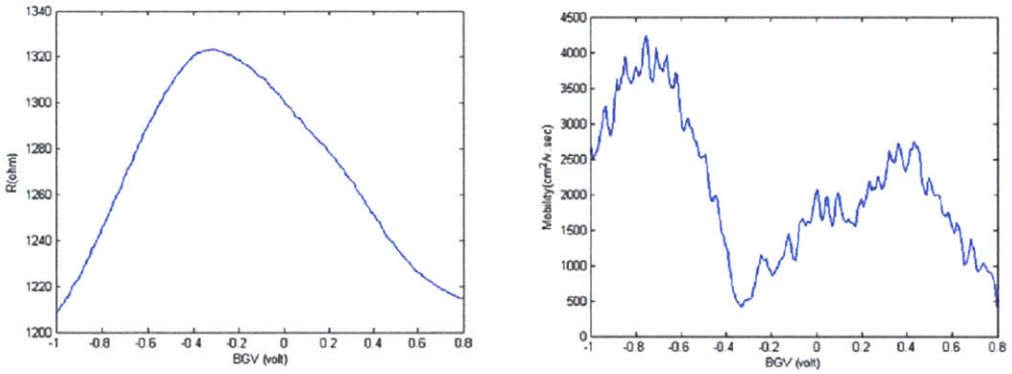

Figure 5-3: Resistance and charge carrier mobility of the device shown in Fig. 5-2 measured as a function of back gate voltage. (Image courtesy of Joel Wang)

charge carriers across junctions of several hundred nanometers wide [11] [6].

The back gate dependence of resistance is shown here for two of our devices. The first device, Fig. 5-2, was written using electron beam lithography with the tri-layer PMMA used in transfer as the resist, and the contacts are sputtered niobium. The flakes are suspended over trenches, and underwent no annealing after transfer. We can see that even without annealing, the Dirac point is very close to zero voltage (Fig. 5-3. The mobility, however, is not that great, only $4000\,cm^2\,V^{-1}\,s^{-1}$. Unfortunately, the device leaked current to the back gate at voltages higher than 1 V or less than -1 V, so a full measurement of the back gate dependence of resistance could not be

Figure 5-4: Suspended graphene Josephson junction device which underwent no annealing before measurement. The device measured is the bottom one (circled in black)

performed.

The second devices, Fig. 5-4, was a flake over trenches with Cr/Au leads evaporated on the sections on top of the substrate to act as leads for current annealing. The purpose of the current annealing is to clean the graphene sample so as to have a clean graphene sample on which we will fabricate graphene Josephson junctions. Comparing the data from before annealing, Fig. 5-5, and after, Fig 5-6, we can see the efficacy of using current annealing to clean the graphene sample and prepare it for the fabrication of Josephson junctions. Unfortunately, the device was destroyed during later steps in the fabrication process. More devices are being fabricated using this method, however, and we hope to see a high mobility niobium-graphene-niobium Josephson junction which will allow us to measure the Josephson effect in graphene in the quantum Hall regime.

5.2 Multiple Andreev Reflection

As described in section 3.5.1, multiple Andreev reflection is an indication of good transparency of the graphene-superconductor interface to Cooper pairs in a Josephson junction. Using the first device shown in the previous section, measurements were taken of the differential resistance of the device as a function of the bias current across

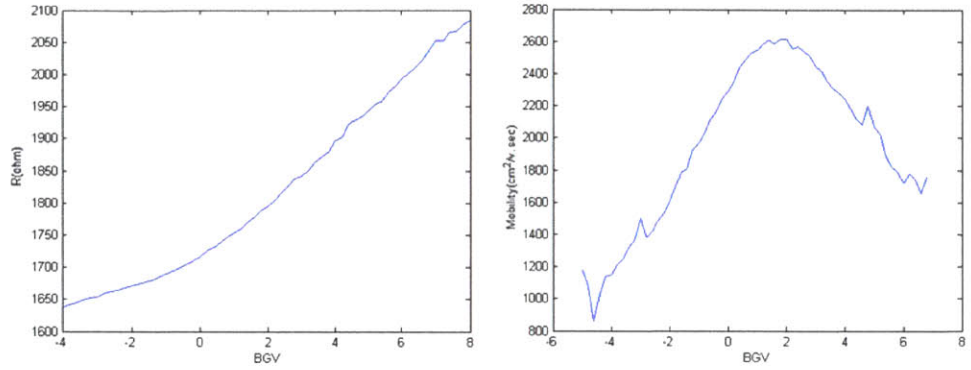

Figure 5-5: Resistance and charge carrier mobility of the device shown in Fig. 5-4 measured as a function of back gate voltage before current annealing. Note the low mobility of the device and distance of the Dirac peak from zero voltage, most likely due to the fact that most of the graphene is not suspended.

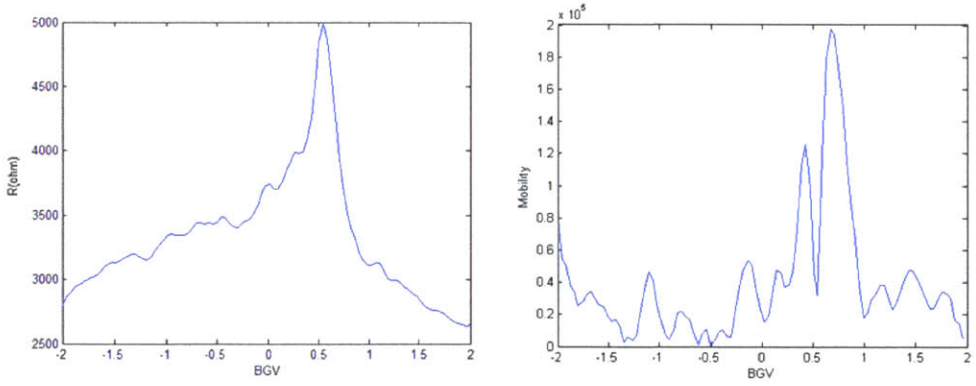

Figure 5-6: Resistance and charge carrier mobility of the device shown in Fig. 5-4 measured as a function of back gate voltage after current annealing. The mobility is a lower bound on the estimate, as the dielectric constant of air, 1, is significantly smaller than the dielectric of silicon, ≈ 12. Thus, the suspended portion has a lower capacitance than the value used in our estimates, and the real mobility could be significantly higher.

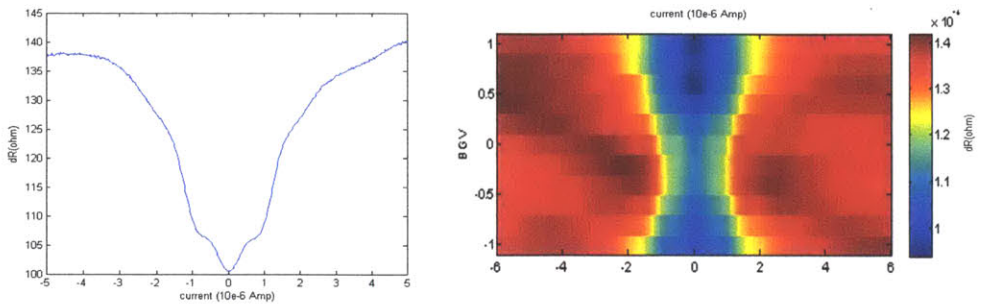

Figure 5-7: Differential resistance vs bias current in the device shown in Fig. 5-2. The left hand plot is for a device with a back gate voltage of -1 V, and the right hand plot shows the device for a series of back gate voltges from -1 V to 1 V. (Images courtesy of Joel Wang)

the junction. To take these measurements, the back gate voltage is first applied via the same method as the previous measurement. Then, a DC current source is connected to the junction to apply the bias current. A lock-in amplifier is again used as another current source, this time applying a small amplitude current signal across the junction and used to measure the resultant voltage change across the junction due to this AC signal. The small perturbation in current acts as our dI, and the resulting voltage perturbation is dV, and so by dividing the amplitude of the output voltage by the amplitude of the input current, we can find $dV/dI = dR$, which is shown in Fig. 5-7 plotted against the DC bias current.

There are four "hitches" in the differential resistance at bias currents $\approx \pm 2\,\mu$A and $\approx \pm 1\,\mu$A, which could be caused by multiple Andreev reflection. Using $1.2\,\text{k}\Omega$ for the resistance of the graphene at back gate voltage -1 V (Fig. 5-3), this corresponds to bias voltages of $\approx \pm 2.4$ mV and $\approx \pm 1.2$ mV, which are close to $2\Delta_{Nb}$ and $2\Delta_{Nb}/2$, where $\Delta_{Nb} = 1.4$ mV is the superconducting gap energy of niobium. Given the relatively high temperature at which these measurements were taken, the evidence of multiple Andreev reflection, despite its weakness, is indicative of both the high quality of our suspended graphene sample as well as the good transparency of our metal-graphene contact. Had this device not been destroyed while trying to fix the back gate leakage, it almost certainly would have displayed the Josephson effect when measured at lower temperatures (tens of mK).

Chapter 6

Conclusion

In this thesis, I have described the start of our study of graphene Josephson junctions in the quantum Hall regime, a previously unexplored experimental regime. Joel and I have been able overcome the challenges associated with suspending and annealing graphene Josephson junctions and fabricate a suspended graphene Josephson junctions which show multiple Andreev reflection at 4 K without any annealing. We have also been able to anneal suspended graphene flakes to achieve mobilities exceeding $200,000\,cm^2\,V^{-1}\,s^{-1}$, and found a fabrication process which can preserve the cleanness of these high mobility flakes through the rest of the fabrication process. Our new fabrication process is highly reproducible and provides a way of creating Josephson junctions with a high critical magnetic field, something that still has not appeared in literature.

Through the combination of our two separate processes, we should be able to create high mobility niobium-graphene-niobium Josephson junctions in the very near future, devices which will allow us to study the interaction between superconductivity and quantum Hall edge states in graphene. In addition to this, we also plan to to study with these devices phenomena such as specular Andreev reflection and strain induced vector potentials (pseudo-magnetic fields) in graphene [14]. The ability to fabricate high mobility graphene Josephson junctions which can withstand high magnetic fields opens the door to many possible experiments, and our general fabrication process for suspended graphene devices could pave the way for more complex devices in the future

to further probe the fascinating properties of graphene.

Bibliography

[1] D. A. Abanin, P. A. Lee, and L. S. Levitov. Spin-Filtered Edge States and Quantum Hall Effect in Graphene. *Physical Review Letters*, 96(17):176803–+, May 2006.

[2] W. Bao, F. Miao, Z. Chen, H. Zhang, W. Jang, C. Dames, and C. N. Lau. Controlled ripple texturing of suspended graphene and ultrathin graphite membranes. *Nature Nanotechnology*, 4:562 566, September 2009.

[3] J. Bardeen, L. N. Cooper, and J. R. Schrieffer. Microscopic theory of superconductivity. *Phys. Rev.*, 106(1):162–164, Apr 1957.

[4] C. W. J. Beenakker. Specular andreev reflection in graphene. *Phys. Rev. Lett.*, 97(6):067007, Aug 2006.

[5] C. W. J. Beenakker. Colloquium: Andreev reflection and klein tunneling in graphene. *Rev. Mod. Phys.*, 80(4):1337–1354, Oct 2008.

[6] K. I. Bolotin, K. J. Sikes, Z. Jiang, M Klima, F. Fudenberg, J Hone, P. Kim, and H. L. Stormer. Ultrahigh electron mobility in suspended graphene. *Solid State Communications*, 146(9-10):351 – 355, 2008.

[7] K. I. Bolotin, K. J. Sikes, Z. Jiang, M. Klima, G. Fudenberg, J. Hone, P. Kim, and H. L. Stormer. Ultrahigh electron mobility in suspended graphene. *Solid State Communications*, 146:351 355, June 2008.

[8] J. Clarke. The Josephson Effect and e/h. *American Journal of Physics*, 38(9):1071–1095, 1970.

[9] Leon N. Cooper. Bound electron pairs in a degenerate fermi gas. *Phys. Rev.*, 104(4):1189–1190, Nov 1956.

[10] C. R. Dean, A. F. Young, I. Meric, C. Lee, L. Wang, S. Sorgenfrei, K. Watanabe, T. Taniguchi, P. Kim, K. L. Shepard, and J. Hone. Boron nitride substrates for high-quality graphene electronics. *Nature Nanotechnology*, 5:722–726, October 2010.

[11] X. Du, I. Skachko, A. Barker, and E. Y. Andrei. Approaching ballistic transport in suspended graphene. *Nature Nanotechnology*, 3:491 495, August 2008.

[12] R. P. Feynman, R. B. Leighton, and M. Sands. *Feynman Lectures on Physics*, volume 3, chapter 21, pages 21–14. Addison-Wesley, Reading, Massachusetts, third printing edition, July 1966.

[13] A. K. Geim and K. S. Novoselov. The rise of graphene. *Nature Materials*, 6(3):183–191, March 2007.

[14] F. Guinea, M. I. Katsnelson, and A. K. Geim. Energy gaps and a zero-field quantum Hall effect in graphene by strain engineering. *Nature Physics*, 6:30–33, January 2010.

[15] H. B. Heersche, P. Jarillo-Herrero, J. B. Oostinga, L. M. K. Vandersypen, and A. F. Morpurgo. Bipolar Supercurrent in Graphene. *Nature*, 446:56–59, March 2007.

[16] W Hu, K. Sarveswaran, M. Lieberman, and Bernstein G. H. Sub-10 nm electron beam lithography using cold development of poly(methylmethacrylate). *Journal of Vacuum Science & Technology B: Microelectronics and Nanometer Structures*, 22(4):1711–1716, 2004.

[17] B. D. Josephson. Possible New Effects in Superconductive Tunnelling. *Physics Letters*, 1:251–253, July 1962.

[18] T. M. Klapwijk, G. E. Blonder, and M. Tinkham. Explanation of subharmonic energy gap structure in superconducting contacts. *Physica B+C*, 109-110:1657 – 1664, 1982.

[19] K. v. Klitzing, G. Dorda, and M. Pepper. New method for high-accuracy determination of the fine-structure constant based on quantized hall resistance. *Phys. Rev. Lett.*, 45(6):494–497, Aug 1980.

[20] L. D. Landau. Zur theorie der phasenumwandlungen ii. *Phys. Z. Sowjetunion*, 11:26–35, 1937.

[21] F. London and H. London. The Electromagnetic Equations of the Supraconductor. *Royal Society of London Proceedings Series A*, 149:71 88, March 1935.

[22] N. D. Mermin. Crystalline order in two dimensions. *Phys. Rev.*, 176(1):250–254, Dec 1968.

[23] J. Moser, A. Barreiro, and A. Bachtold. Current-induced cleaning of graphene. *Applied Physics Letters*, 91(16):163513, 2007.

[24] K. S. Novoselov, A. K. Geim, S. V. Morozov, D. Jiang, M. I. Katsnelson, I. V. Grigorieva, S. V. Dubonos, and A. A. Firsov. Two-dimensional gas of massless Dirac fermions in graphene. *Nature*, 438:197 200, November 2005.

[25] K. S. Novoselov, A. K. Geim, S. V. Morozov, D. Jiang, Y. Zhang, S. V. Dubonos, I. V. Grigorieva, and A. A. Firsov. Electric Field Effect in Atomically Thin Carbon Films. *Science*, 306:666–669, October 2004.

[26] L. E. Ocola and A. Stein. Effect of cold development on improvement in electron-beam nanopatterning resolution and line roughness. *Journal of Vacuum Science Technology B: Microelectronics and Nanometer Structures*, 24:3061–3066, 2006.

[27] R. Peierls. Quelques propriétés typiques des corps solides. *Ann. I. H. Poincaré*, 5:197–222, 1935.

[28] J. W. Rohlf. *Modern Physics from α to Z^0*, chapter 15. Wiley, March 1994.

[29] D. J. Scalapino. Josephson Effects. In R. G. Lerner and G. L. Trigg, editors, *Encyclopedia of Physics*, pages 479–481. Addison-Wesley, Reading, MA, 1981.

[30] J. Tworzydło, B. Trauzettel, M. Titov, A. Rycerz, and C. W. J. Beenakker. Sub-poissonian shot noise in graphene. *Phys. Rev. Lett.*, 96(24):246802, Jun 2006.

[31] K. von Klitzing. Developments in the quantum Hall effect. *Royal Society of London Philosophical Transactions Series A*, 363:2203–2219, September 2005.

[32] P. R. Wallace. The band theory of graphite. *Phys. Rev.*, 71(9):622–634, May 1947.